

# SPDFusion: An Infrared and Visible Image Fusion Network Based on a Non-Euclidean Representation of Riemannian Manifolds

Huan Kang, Hui Li, Tianyang Xu, *Member, IEEE*, Rui Wang, Xiao-Jun Wu\*, and Josef Kittler, *Life Member, IEEE*

**Abstract**—Euclidean representation learning methods have achieved commendable results in image fusion tasks, which can be attributed to their clear advantages in handling with linear space. However, data collected from a realistic scene usually have a non-Euclidean structure, where Euclidean metric might be limited in representing the true data relationships, degrading fusion performance. To address this issue, a novel SPD (symmetric positive definite) manifold learning framework is proposed for multi-modal image fusion, named SPDFusion, which extends the image fusion approach from the Euclidean space to the SPD manifolds. Specifically, we encode images according to the Riemannian geometry to exploit their intrinsic statistical correlations, thereby aligning with human visual perception. Actually, the SPD matrix underpins our network learning, with a cross-modal fusion strategy employed to harness modality-specific dependencies and augment complementary information. Subsequently, an attention module is designed to process the learned weight matrix, facilitating the weighting of spatial global correlation semantics via SPD matrix multiplication. Based on this, we design an end-to-end fusion network based on cross-modal manifold learning. Extensive experiments on public datasets demonstrate that our framework exhibits superior performance compared to the current state-of-the-art methods.

**Index Terms**—image fusion, cross-modal manifold learning, statistical correlation, SPD manifold.

## 1 INTRODUCTION

WITH the development of multi-modal sensor technology, image fusion is playing an increasingly important role in the field of computer vision. This task integrates image data from different imaging sensors to obtain richer and more accurate information about the scene. Multi-modal image fusion has many applications in various practical fields such as medical imaging [1] [2], remote sensing monitoring [3] [4], semantic segmentation [5], and military reconnaissance, etc.

In the past few decades, many effective image fusion methods have been developed, which can roughly be divided into two categories: image fusion techniques based on traditional methods and image fusion techniques based on deep learning networks.

The introduction of many traditional methods such as multi-scale transformation [6] and low-rank representation [7] [8] has significantly contributed to the task of image fusion. However, these methods typically rely on indepen-

dent representations of the original features or some other forms of feature combination, such as direct use of pixel values, application of local descriptors, or the construction of histograms, which may not express the interrelationships between features effectively.

Compared to the traditional image processing techniques, deep learning architectures [9] [10] [11] have shown significant effectiveness in the field of image fusion thanks to their superior ability in extracting high-level feature, learning of nonlinear transformations, and in complex pattern recognition. In the current research, methods based on Convolutional Neural Networks (CNN) [12] have shown to be effective in the field of image fusion. These methods adopt an end-to-end learning approach [13] that trains the network directly from pairs of input images to produce the fused result, capturing image characteristics at different levels from low-level edges and textures to higher-level semantic content. However, CNN extracts local features through convolution operations in the local receptive field, and this often leads to the neglect of long-range dependencies in the image, which is disadvantageous for achieving high-quality image fusion. For instance, in tasks such as depth-of-field extension or multi-focus image fusion [14] [15], maintaining relations between foreground and background usually requires considering contextual information from the entire image scene.

In 2021, the Vision Transformer (ViT) [16] appeared as a revolutionary architecture, shifting the deep learning paradigm from traditional convolution operations to processing images by dividing them into fixed-size tokens, which can capture long-range dependencies between image segments. Subsequent applications, especially in image

- This work is supported in part by the National Key Research and Development Program of China (2023YFF1105102, 2023YFF1105105), the National Natural Science Foundation of China (62020106012, 62332008, 62106089, 62336004, 62306127), the 111 Project of Ministry of Education of China (B12018), and the UK EPSRC (EP/N007743/1, MURI/EP/SRC/DSTL, EP/R018456/1).
- Huan Kang, Hui Li, Tianyang Xu, Rui Wang and Xiao-Jun Wu are with the School of Artificial Intelligence and Computer Science, Jiangnan University, Wuxi 214122, China. E-mail: Shaoyun2023@126.com, lihui.cv@jiangnan.edu.cn, tianyang\_xu@163.com, cs\_wr@jiangnan.edu.cn, xiaojun\_wu\_jnu@163.com (corresponding author)
- Josef Kittler is with the Centre for Vision, Speech and Signal Processing, University of Surrey, Guildford, GU2 7XH, UK. E-mail: j.kittler@surrey.ac.uk

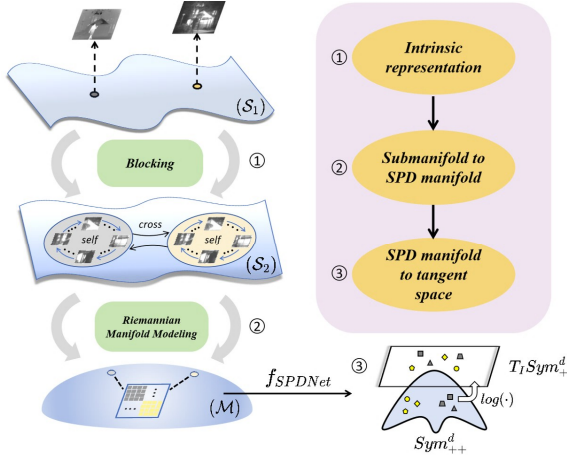


Fig. 1: A new modeling approach based on the representation of Riemannian manifold. We divide the images from two sources of data into patches, allowing the network to focus on local details and global context information. Where the cross-modal image pairs are considered to be on the manifold  $S_1$ , while the manifold  $S_2$  where the patches reside can be regarded as a manifold structure that is homeomorphic to  $S_1$ .  $\mathcal{M}$  denotes the SPD Riemannian manifold,  $Sym^d_{++}$  represents the symmetric positive definite manifold, and  $T_Sym^d_{++}$  is the tangent space of the SPD manifold at the  $d \times d$  identity matrix  $I$ .

fusion tasks, such as TransMEF [17] and SwinFusion [18], capitalized on this method’s powerful capabilities. Despite the significant progress, these models overly focus on the self-attention mechanism itself, sacrificing cross-modal interaction processes. Yet, in fusion tasks, such associative information is crucial [19] [20].

In computer vision, data often contains rich intrinsic structures and hidden associations, especially in multi-modal fusion tasks. Samples within a modality are highly correlated in the feature space, while the relationship between samples across different modalities is weaker.

To tap the implicit interactions and dependencies of data from different modalities, bearing in mind the intrinsic non-Euclidean manifold structure of images, we propose an infrared and visible light image fusion algorithm based on the SPD manifold. This model applies Riemannian manifold [11] to the image fusion task for the first time, mining the raw pixel characteristics and their statistical relationships to guide the fusion results. This method not only preserves the inherent geometric properties of image data on the Riemannian manifold but also facilitates the interaction of cross-modal image correlation information. On one hand, we design an SPD manifold attention module (SPDAM), which, through the introduction of a mixed attention mechanism, strengthens the statistical correlation within each modality and across the different modalities. On the other hand, geometric computations on Riemannian manifolds enable a more refined capture and utilization of the spatial nonlinear characteristics, thereby providing a better fit to the intricate geometric structure inherent in image data. Based on this, we model the covariance among image patches, effectively achieving the learning of global correlation relationships,

and the main idea of the proposed method is shown in Fig. 1. Our main contributions are as follows:

1. For the first time, the Riemannian manifold is introduced into the image fusion task. The proposed method exhibits unique advantages due to its adaptation to the non-Euclidean distribution of image data and the consideration of its intrinsic geometric structure.
2. A novel manifold attention module has been designed, which reflects the global correlation between features through the covariance of pixel point representations. As the manifold network continuously updates, it further strengthens semantic associations, effectively guiding the fusion task.
3. A novel cross-modal fusion strategy has been introduced, which integrates features from different modalities on the SPD manifold, enhancing the inter-modality correlations and improving the fusion effectiveness.
4. Experimental results on public benchmark datasets indicate that our fusion network exhibits superior fusion performance compared to existing fusion methods.

## 2 RELATED WORKS

In this section, we explore neural networks based on covariance matrices as well as SPD neural networks constructed upon them, and also elaborate on network modules based on spatial attention.

### 2.1 Covariance Matrix

The covariance matrix is an important tool for describing the statistical linear dependence between variables in a dataset [21]. It offers a comprehensive perspective on multivariate data in terms of second-order moment statistics and provides a mathematically rigorous method for quantitative modeling of the interrelationships between variables.

The potential of the covariance matrix has been effectively utilized in many branches of statistics. However, its application in pattern recognition is relatively rare. It has been proven that covariance matrices are effective in various scenarios. For example, in image set classification [22] [23], the covariance matrix can represent the statistical characteristics of a set of images and characterize the image set as a distribution of feature points. This property of covariance can be used to perform more complex tasks, such as recognizing facial expressions or motion patterns. In medical imaging [24], the covariance matrix is used to capture morphological changes in various tissues or structures, and by studying these changes, disease characteristics can be revealed, helping doctors make more accurate diagnoses.

However, Riemannian networks based on covariance matrices are mainly applied to classification problems, and the features extracted by them often do not fully meet the specific requirements of image fusion tasks. Additionally, the effect of regional correlations between inter-modal data on the fusion outcome has not been fully understood and studied, particularly in tasks involving multi-modal data fusion, such as analyzing experimental data, multi-spectral satellite images, or multi-modal medical images. These correlations can reveal the intrinsic connections between the data of different modalities, such as the scene features

captured by different sensors, or help distinguish unrelated information. This is crucial for building accurate fusion models and for understanding the performance of the data after fusion.

## 2.2 The Basic Layer of SPD Neural Network

Since traditional machine learning and classification methods generally assume the Euclidean space, these methods are not suitable for dealing with the nonlinear structure of covariance matrices, as they fail to take into account the intrinsic geometric characteristics of data points on the manifold. Fortunately, researchers have proposed an innovative neural network architecture: SPDNet [25], which is specifically designed to adapt to the unique features of SPD matrices. In its overall structure, it is similar to traditional Euclidean neural networks, including transformations, nonlinear activations, and the final classification stage. The difference lies in the fact that the SPDNet architecture includes specialized layers to ensure the outputs remain on the manifold, utilizing operations such as Riemannian metric, exponential and logarithmic mappings, as well as geodesic distances compatible with manifold geometry [26]. The basic layers can be divided into three categories:

**BiMap Layer:** This layer is designed to reduce the dimension and enhance the discriminative features while preserving the SPD matrix characteristics of the data. By applying a bilinear mapping, the BiMap layer can map SPD matrices from a high-dimensional SPD manifold to another low-dimensional SPD manifold, while maintaining the geometric structure and positive properties of the data. The specific mapping formula is:

$$X_k = f_b(X_{k-1}; W_k) = W_k X_{k-1} W_k^T \quad (1)$$

Where  $X_k$  is the newly mapped SPD matrix,  $X_{k-1}$  is the SPD matrix input at the  $k$ -th layer, belonging to the manifold of symmetric positive definite matrices,  $W_k$  is the transformation matrix, which should be row full-rank, and if its columns are orthogonal,  $W_k$  belongs to the compact Stiefel manifold  $St(d_k, d_{k-1})$ , where  $d_k$  is the dimension of the mapped SPD matrix after the transformation, typically smaller than  $d_{k-1}$ , to achieve dimensionality reduction.

**ReEig Layer:** It introduces a nonlinear activation function within SPDNet while preserving the SPD matrix structure. The role of this layer is similar to the ReLU activation function, which increases the complexity of decision boundaries and enhances the model's expressive capacity. Similarly, the ReEig layer introduces non-linearity to the Riemannian manifold by rectifying eigenvalues to a lower bound threshold, preventing degradation issues associated with very small eigenvalues, and allowing the model to capture more complex and abstract features. The formula is as follows:

$$X_k = f_r^{(k)}(X_{k-1}) = U_{k-1} \max(\epsilon I, \Sigma_{k-1}) U_{k-1}^T \quad (2)$$

where the matrices  $U_{k-1}$  and  $\Sigma_{k-1}$  are the results of performing an eigenvalue decomposition (EIG) on  $X_{k-1}$ , such that  $X_{k-1}$  is factored as  $U_{k-1} \Sigma_{k-1} U_{k-1}^T$ ,  $\epsilon$  denotes a rectification threshold,  $I$  represents an identity matrix, and

$\max(\epsilon I, \sigma_{k-1})$  is obtained by element-wise maximum comparison, with the diagonal entries determined as follows:

$$A(i, i) = \begin{cases} \sum_{k-1}(i, i) & \text{if } \sum_{k-1}(i, i) > \epsilon \\ \epsilon & \text{if } \sum_{k-1}(i, i) \leq \epsilon \end{cases} \quad (3)$$

where  $A$  is a diagonal matrix.

The key to the LogEig layer is that it offers a means to effectively "straightening" the curved manifold space into a flat Euclidean space while preserving the SPD property (positive-definiteness) by performing logarithmic operations on the eigenvalues obtained from an EIG (eigenvalue decomposition) of the matrix. This makes linear operations feasible in the Euclidean space.

$$X_k = f_l^{(k)}(X_{k-1}) = \log(X_{k-1}) = U_{k-1} \log(\Sigma_{k-1}) U_{k-1}^T \quad (4)$$

For a SPD matrix  $X_{k-1}$ , one first performs the eigenvalue decomposition  $X_{k-1} = U_{k-1} \Sigma_{k-1} U_{k-1}^T$ , where  $U_{k-1}$  is an orthogonal matrix comprised of eigenvectors, and  $\Sigma_{k-1}$  is a diagonal matrix of corresponding eigenvalues. Following this, the logarithm of the diagonal elements of  $\Sigma_{k-1}$  is computed to obtain the diagonal matrix of log-eigenvalues  $\log(\Sigma_{k-1})$ . Finally, the SPD matrix  $X_k$  is reconstructed through  $U_{k-1} \log(\Sigma_{k-1}) U_{k-1}^T$ , thus  $X_k$  represents  $X_{k-1}$  in the log domain.

## 2.3 Deep Learning Tasks Based on Spatial Attention

The concept of attention mechanisms is derived from the basic characteristics of the human perception system. It is well known that human vision does not uniformly process the entire field of view; instead, it prioritizes those parts that are most informative. This selective focus allows us to efficiently manage our limited cognitive resources to better understand our environment.

In the fields of deep learning and computer vision, attention mechanisms attempt to mimic this selective visual focus. The traditional Convolutional Neural Networks (CNNs) [27] [28] typically treat all parts of the input equally, which may not be the most efficient method when dealing with complex or cluttered data. With the development of large-scale classification tasks and other vision tasks, researchers began to explore how to make CNNs focus more on important local information in the image, similar to human vision.

In image processing tasks, spatial attention and channel attention are two common types of attention. Spatial attention focuses on the importance of specific areas within an image, while channel attention focuses on the importance of feature channels.

Hu et al. proposed a structural unit called SEBlock (Squeeze-and-Excitation block) [29] based on the inter-relationships between channels. It dynamically calibrates channel feature responses by explicitly modeling the dependencies between channels. However, the SEBlock's approach is limited in that it uses global average pooling to calculate channel attention, which may not be the optimal feature for inferring fine-grained channel attention, and it does not consider the equally important spatial attention, thus failing to achieve semantic-level perception of the context of objects in a scene and their spatial relationships.

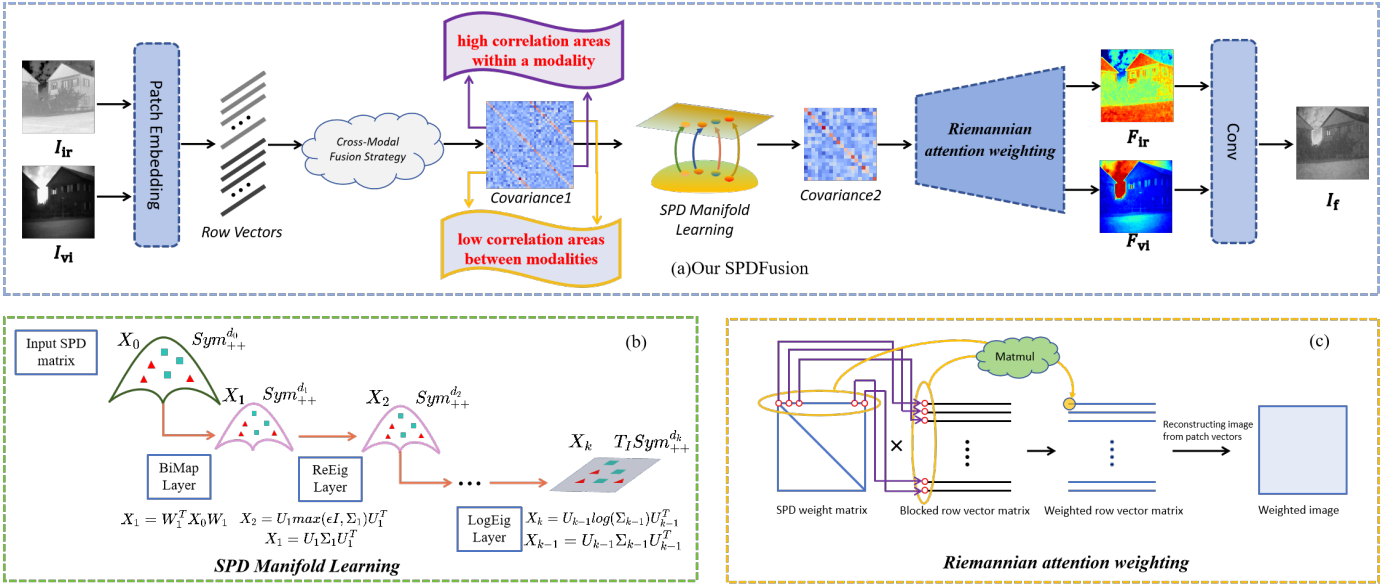


Fig. 2: The workflow of our SPDFusion: (a) The main framework of our fusion network is defined. (b) Details of manifold learning. (c) The Riemannian attention weighting operation, which is tailored specifically for our fusion task.

CBAM (Convolutional Block Attention Module) [30] introduces spatial attention on top of this. It is a lightweight attention module that refines the input feature maps by sequentially applying channel and spatial attention mappings. Unlike channel attention, spatial attention focuses on the “where” question in the input feature maps, identifying which areas of the image parts are information-rich, in order to emphasize or suppress these areas. This is usually achieved by processing each spatial location of the feature maps to generate a spatial attention map that indicates the importance of each location.

In traditional Euclidean space attention mechanisms, the attention weights are calculated through dot-product operations between query and key vectors. This method shows limitations when dealing with data that contains complex manifold structures. To address this, our proposed manifold attention expands the traditional Euclidean attention to data representations based on symmetric positive definite manifolds. The key innovation is to learn latent representational associations between two modalities through covariance modeling, thereby establishing a new paradigm for representing global features statistically. More critically, this framework is optimized within a Riemannian manifold space, allowing the algorithm to handle non-linear structures in a more natural manner, and preserving the geometric relationships and topological properties of the data.

### 3 THE PROPOSED METHOD

In this section, we provide a detailed description of the SPDFusion network framework, the cross-modal SPD fusion strategy, and the SPD Manifold Attention Module, as well as an explanation of our training process and loss function.

#### 3.1 The Network Framework

The proposed fusion network (SPDFusion) architecture is shown in Fig. 2(a), the source images are first encoded into overlapping patch vectors, and then the covariance of the encoded patch row vector matrix is computed via the “Cross-Modal Fusion Strategy” to detect statistical relationships between different patches. Through covariance computation, we not only capture the feature relationships within a single modality but also use algorithms to highlight low-correlation yet information-rich features across modalities. (This part will be explained in detail in Section 3.2.) In this way, the statistical representations within and between modalities are not only based on the original image space but also incorporate deep statistical information across multiple modalities, providing a rich data basis for manifold learning. Furthermore, to ensure the non-Euclidean geometric structure of the image is preserved, our designed manifold learning module completes cross-modal attention interaction within the Riemannian space, and the learned weight coefficients are “flattened” back to Euclidean space through logarithmic mapping. Specifically, we designed a Riemannian attention weighting module based on the principle of convolution operations, injecting manifold statistical relevance into the image. Finally, the weighted image features are subjected to deep feature extraction through a series of convolutional layers to obtain the final fusion result.

The source images  $I_{ir}$  and  $I_{vi}$  are the infrared image and visible light image, respectively. To acquire a global spatial information representation, we first segment each image into patches with overlapping regions. For each patch, we arrange all the pixels in a sequential order to form a row vector. For each image modality, a matrix of row vectors corresponding to the rearranged image block matrices can be obtained. Specifically, let  $P_{ir}$  and  $P_{vi}$  be the patch sets of the infrared and visible light images, with  $p_{ir_i}$  being the  $i$ -th

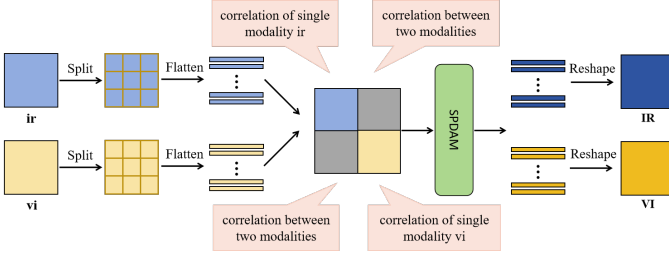


Fig. 3: The framework of our fusion strategy.

patch of  $I_{ir}$ , and  $p_{vi}$  being the  $i$ -th patch of  $I_{vi}$ . For each  $p_{ir_i}$  in  $P_{ir}$ , we can construct the row vector  $x_{ir_i}$ . And for each  $p_{vi_i}$  in  $P_{vi}$ , we can also construct the row vector  $x_{vi_i}$ . Eventually, we obtain the matrix of row vectors  $X_{ir}$  for the infrared image and  $X_{vi}$  for the visible light image, which can be expressed as:

$$X_{ir} = \begin{bmatrix} x_{ir_1} \\ x_{ir_2} \\ \vdots \\ x_{ir_n} \end{bmatrix}, \quad X_{vi} = \begin{bmatrix} x_{vi_1} \\ x_{vi_2} \\ \vdots \\ x_{vi_n} \end{bmatrix} \quad (5)$$

where  $n$  denotes the total number of patches.

subsequently, we computed the covariance matrix "Covariance1" between the vectorized patches, which encapsulates the correlation representation information of different regions in the image, denoted as  $S$ . To ensure that the covariance matrix satisfies the basic properties of the SPD manifold, we perform an SVD on this symmetric semi-definite matrix, and add a small positive perturbation term  $\epsilon$  to the eigenvalue matrix, to ensure that all the eigenvalues are greater than zero:

$$Q = U(S + \epsilon * \text{tr}(S))V^T \quad (6)$$

where  $\epsilon$  is a very small positive number, usually set as 0.001.  $U$  and  $V^T$  represent the orthogonal matrices obtained from the SVD of the original positive semi-definite matrix, respectively.  $S$  represents the diagonal matrix obtained by singular value decomposition, and the resultant matrix  $Q$  belongs to an SPD manifold  $X_0$  in the Riemannian space.  $X_0$  goes through the SPD manifold network to learn the deep statistical information of different modalities, and embeds the learned feature manifold into the Euclidean space for attention weighting:

$$\phi_{S_i} = X_k \phi_{row}, i \in \{ir, vi\} \quad (7)$$

where  $X_k$  represents the weight matrix, which can also be represented as "Covariance2".  $\phi_S$  represents the final feature map obtained, and  $\phi_{row}$  represents the matrix of row vectors.

In order to allow the model to extract and learn higher-level feature representations from the input data, consecutive convolutional layers and LeakyReLU activation functions are added after obtaining the feature map by SPDAM. At the same time, by using different filters to extract features at various levels, higher-level abstract representations are established, and deep features of the two modalities are fused and decoded:

$$F_f = \text{conv}_{3 \times 3}(\text{cat}(\phi_{S_{ir}}, \phi_{S_{vi}})) \quad (8)$$

Following the steps mentioned above, we obtain the final fusion result  $F_f$ .

### 3.2 Cross Modal SPD Fusion Strategy

The core of this strategy is to use a structured feature map stacking method, in which the feature maps of two different modalities are arranged vertically for interaction within the same dimensional space. Specifically, the two source images are firstly divided into patches and flattened into vectors as shown in Fig. 3. In our work, the patch size, the stride between blocks, and the overlapping block size are set to 16, 8, and 8, respectively. After the patches are flattened, we obtain the row vector matrices  $X_{ir}$  and  $X_{vi}$ , corresponding to different modalities. The process of vertical arrangement can be described as constructing a new stacked matrix  $X_{stacked}$ , which merges  $X_{ir}$  and  $X_{vi}$  as follows:

$$X_{stacked} = \begin{bmatrix} X_{ir} \\ X_{vi} \end{bmatrix} \quad (9)$$

where  $X_{ir} \in \mathbb{R}^{m \times n}$ ,  $X_{vi} \in \mathbb{R}^{p \times n}$  and  $X_{stacked} \in \mathbb{R}^{(m+p) \times n}$ . Here  $m$  and  $p$  denote the number of the row vectors for the two modalities, and  $n$  represent the dimension of the row vector. For any two rows  $X_i$  and  $X_j$  ( $i, j = 1, 2, \dots, m+p, i \neq j$ ) in  $X_{stacked}$ , the covariance representation between the row vectors can be formulated as:

$$\text{Cov}(X_i, X_j) = \frac{1}{n-1} \sum_{k=1}^n (X_{ik} - \bar{X}_i)(X_{jk} - \bar{X}_j)^T \quad (10)$$

where  $\bar{X}_i$  and  $\bar{X}_j$  represent the average of all observed feature values for the  $i$ -th patch and the  $j$ -th patch, respectively.

Then, a composite covariance matrix is constructed, serving as a vehicle for analyzing the collaborative variation trends between composite data points on the entire high-dimensional data manifold. The matrix is divided into four quadrant blocks:

$$C_X = \begin{bmatrix} C_{X_{ir}} & C_{X_{ir}X_{vi}} \\ C_{X_{vi}X_{ir}} & C_{X_{vi}} \end{bmatrix} \quad (11)$$

Among them,

$$C_{X_{ir}} = \frac{1}{n-1} \sum_{k=1}^n (X_{ir_k} - \bar{X}_{ir})(X_{ir_k} - \bar{X}_{ir})^T \quad (12)$$

$$C_{X_{vi}} = \frac{1}{n-1} \sum_{k=1}^n (X_{vi_k} - \bar{X}_{vi})(X_{vi_k} - \bar{X}_{vi})^T \quad (13)$$

where  $C_{X_{ir}}$  and  $C_{X_{vi}}$  are the covariance matrices of the patches within  $X_{ir}$  and  $X_{vi}$  themselves, representing the self-correlation characteristics within a single modality. Simultaneously,

$$C_{X_{ir}X_{vi}} = C_{X_{vi}X_{ir}} = \frac{1}{n-1} \sum_{k=1}^n (X_{ir_k} - \bar{X}_{ir})(X_{vi_k} - \bar{X}_{vi})^T \quad (14)$$

where  $C_{X_{ir}X_{vi}}$  and  $C_{X_{vi}X_{ir}}$  represent the covariance matrices between  $X_{ir}$  and  $X_{vi}$ , and  $C_{X_{vi}X_{ir}}$  is the transpose of  $C_{X_{ir}X_{vi}}$ , representing the cross-modal covariance computation, which reveals the relationship between the two modalities.

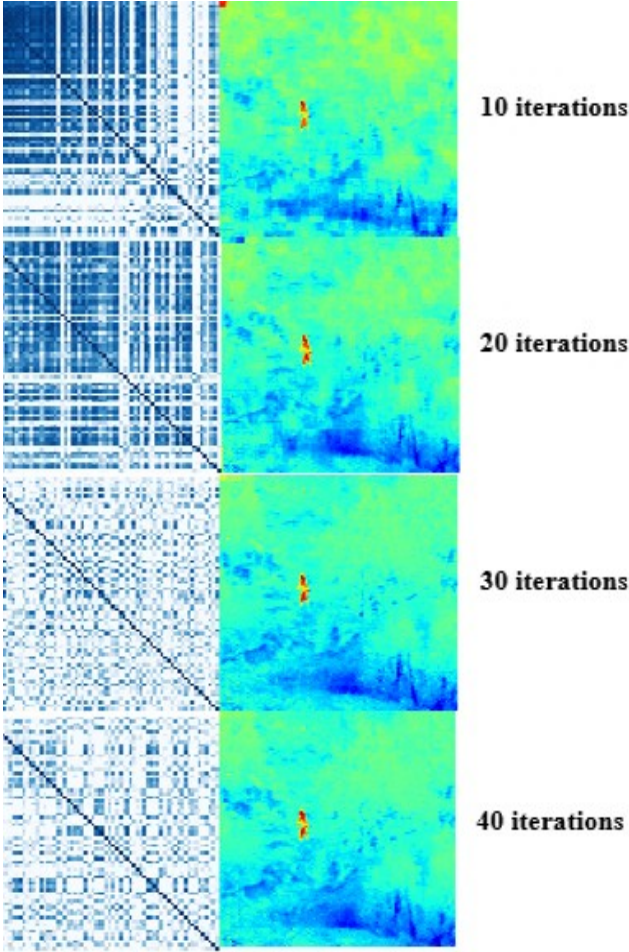


Fig. 4: Visualization of the training results on the manifold under different iteration counts. The first column represents the changes in the Riemannian attention weight matrix, while the second column shows the intermediate results of the fusion.

The covariance matrix  $C_X$  reveals the principle of mutual distribution of points on high-dimensional manifolds from a statistical perspective, explicitly expressing the dependence between different feature points within the SPD manifold. As a key component of cross-modal fusion, it breaks away from the traditional fusion strategy of simply adding through Euclidean distance, providing a new perspective for understanding the non-Euclidean interactions between various modal data.

Once these advanced relational representations are obtained, the model integrates them with the input features to derive the modality-associated enhanced features IR and VI, thereby attracting the attention of the neural network. Furthermore, through gradient backpropagation on the manifold, the model continuously refines the parameters of the SPD matrix to facilitate cross-fusion.

### 3.3 Manifold Learning Network

To facilitate the understanding, we first provide a brief introduction to SPD Riemannian geometry. Firstly, the SPD network is strictly defined on the SPD manifold  $Sym_{++}^{d_k}$ , which is formed by a set of  $d_k$ -dimensional SPD matrices.

These matrices are used to capture statistical correlations between different modes. Here,  $X_{k-1} \in \mathbb{R}^{d_{k-1} \times d_{k-1}}$  denotes the input SPD matrix of the  $k$ -th layer.

As shown in Fig. 2(b), the process of SPD matrix learning starts with a bidirectional mapping layer, known as the BiMap layer, which encodes the global structure of  $X_0$  as well as the complex inter-modal correlations. Through the bidirectional linear mapping, the high-dimensional SPD matrix is gradually transformed into a more compact, lower-dimensional representation, denoted as  $X_1$ , aiming to merge the fine-grained interactions between different modes into a more discriminative low-dimensional SPD manifold.

Subsequently, the ReEig layer obtains a new representation  $X_2$  by performing a nonlinear transformation based on eigenvalue regularization. The key function of this layer is to endow the network with the capability of nonlinear learning while preserving the Riemannian manifold properties of the data. This significantly contributes to the facilitation of more effective SPD parameter learning to a certain extent.

After a series of BiMap and ReEig operations, a set of SPD matrices are obtained which inherently maintain their Riemannian geometric characteristics, and through the logarithmic operation of the LogEig layer, data points on the SPD manifold are mapped to the tangent space at the identity matrix  $T_I Sym_{++}^{d_k}$  to facilitate traditional Euclidean computations. Then, not only are the cross-modal features integrated on the manifold, but the phase information of the SPD matrices is also preserved. Fig. 4 displays the SPD matrix during the network training.

Accompanied this learning process, the neural network continuously performs gradient descent on the complex Riemannian manifold. Utilizing the training-derived SPD manifold weight parameters, we guide the extraction of highly correlated non-Euclidean features, thereby facilitating the cross-fusion of different modalities.

### 3.4 SPD Manifold Attention Module

Following the conventional spatial attention mechanism, we introduce a symmetric positive definite attention module (SPDAM), which hinges on exploiting global semantic associations intrinsic to Riemannian manifolds for enhanced attention modeling. The core of SPDAM lies in its adept usage of a covariance matrix that not only encapsulates symmetry and positive definiteness, but also facilitates the reallocation of manifold attention weights in the Euclidean space.

Central to our method is the concept that points within the SPD manifold, through the innovative deployment of SPDAM, are effectively "flattened" or linearized, enabling their approximation within a Euclidean framework. Mathematically, this transformation can be conceptualized as mapping points  $p$  on the manifold  $M$  through a function  $f : M \rightarrow \mathbb{R}^d$  that linearizes these points within the Euclidean space  $\mathbb{R}^d$ .

Moreover, each pixel in SPD features represents the statistical correlation between feature dimensions, which is a global relationship and can be used as a weight to weight the original image features. In addition, the learning of weight parameters in this article is carried out in the intrinsic space of the data, so the learned weights may be more reasonable.

The ablation experiment in the following text also supports our speculation.

As illustrated on the Fig. 2(c), the element at row  $i$  and column  $j$  in the symmetric matrix generated by our SPD network can be viewed as the statistical correlation between the  $i$ -th patch and the  $j$ -th patch. By multiplying the learned weight matrix with the blocked row vector matrix, the weighted matrix reflects the aggregation of covariance weights of the  $j$ -th feature (i.e., the  $j$ -th pixel position) in the  $i$ -th patch with the same feature in all patches across the image. More specifically, it captures the information aggregation achieved by weighting local features in the global context through the covariance relationships.

Through this natural weighting transition, the spatial features on the manifolds of infrared and visible light modalities are extracted and enhanced, which further improves the fusion network’s capability in representing global and local associative information.

### 3.5 Loss Function

Our SPDFusion is constrained by int loss  $L_{int}$ , grad loss  $L_{grad}$ , structure similarity loss  $L_{ssim}$  and covariance loss  $L_{cov}$ . This is done to enable the network to further enhance semantic information through the correlation between deep features, while learning the color brightness information and texture details in the image. The total loss function  $L_{total}$  is defined as follows:

$$L_{total} = L_{int} + \alpha L_{grad} + \beta L_{ssim} + \gamma L_{cov} \quad (15)$$

$L_{int}$  calculates the difference between the generated image and the target image at the pixel level. It reflects the difference in intensity between images, and is defined as:

$$L_{int} = \frac{1}{HW} \| I_f - \max(I_{ir}, I_{vis}) \|_1 \quad (16)$$

where  $H$  and  $W$  respectively represent the height and width of the image,  $\max(\cdot)$  signifies taking the maximum value of each element, and  $\| \cdot \|_1$  is  $l_1$ -norm.

At the same time, we expect the fusion result to contain more detailed textures, and constrain the image from the changes in gradient, as shown below:

$$L_{grad} = \frac{1}{HW} \| |\nabla I_f| - \max(|\nabla I_{ir}|, |\nabla I_{vis}|) \|_1 \quad (17)$$

where  $\nabla$  is the Sobel operator, and  $|\cdot|$  represents the absolute value operation.

The SSIM loss is a loss function based on the Structural Similarity Index Measure (SSIM), which is used to measure the similarity of two images. Unlike pixel loss, which directly compares pixel values, SSIM considers three relatively independent dimensions: brightness, contrast, and structure. This is closer to the perceptual characteristics of the human visual system. It is defined as:

$$L_{ssim} = (1 - ssim(I_f, I_{vis})) + (1 - ssim(I_f, I_{ir})) \quad (18)$$

where  $SSIM(\cdot)$  represents the structural similarity between two images. The larger it is, the higher the structural similarity between the fused image and the source image.

Furthermore, to restrain the highly correlated features of the image, we employ VGG-16 [31], trained on ImageNet,

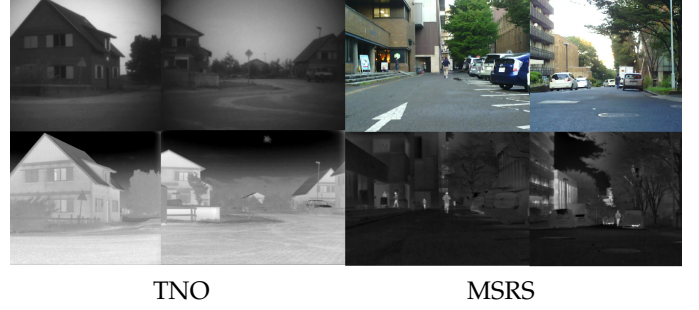


Fig. 5: The examples of two datasets: TNO and MSRS.

to extract features. The third and fourth layers of the VGG network are selected to devise the loss function, which allows us to capture a more abstract characterization of the correlations.  $L_{cov}$  is defined as follows:

$$L_{cov} = \sum_{k=3}^4 \| Cov(\phi(I_f)^k) - Cov(\phi(I_{ir})^k) \|_1 \quad (19)$$

Here,  $Cov(\cdot)$  denotes the covariance matrix of the feature map. Its diagonal elements represent the auto-correlation of each feature appearing in the image, while the off-diagonal elements indicate the correlations between different features.

## 4 EXPERIMENTS AND ANALYSES

In this section, we introduce the fusion results and the analysis of our method. Initially, the SPDFusion experimental settings are presented, followed by ablation studies that reveal the effectiveness of the proposed fusion method and of the SPD attention module. The implementation details are described for repeatability. SPDFusion is benchmarked against leading methods in image fusion tasks, supported by qualitative and quantitative experimental analyses. Finally, the ablation experiments relating to our method are presented and discussed, and these ablation experiments were all conducted on the TNO dataset.

### 4.1 Experimental Settings

In this section, we discuss the datasets, parameter settings, comparative methods, and quantitative metrics used in our approach respectively.

#### 4.1.1 Datasets

In our work, we selected 1083 pairs of corresponding infrared and visible light images from the MSRS dataset [32] as training data, and some instances from the dataset are shown in Fig. 5. The size of the training images is standardized to 256×256 pixels. During the testing phase, we use 40 pairs of images from TNO [33] and 361 pairs of images from MSRS as the test sets, respectively. The dimensions of the test images are typically not fixed.

#### 4.1.2 Parameter Setting

We implemented the algorithm using Pytorch. In the training phase, an end-to-end strategy was employed to train the model on an NVIDIA TITAN RTX GPU. Different optimizers were set for the manifold module and the convolutional

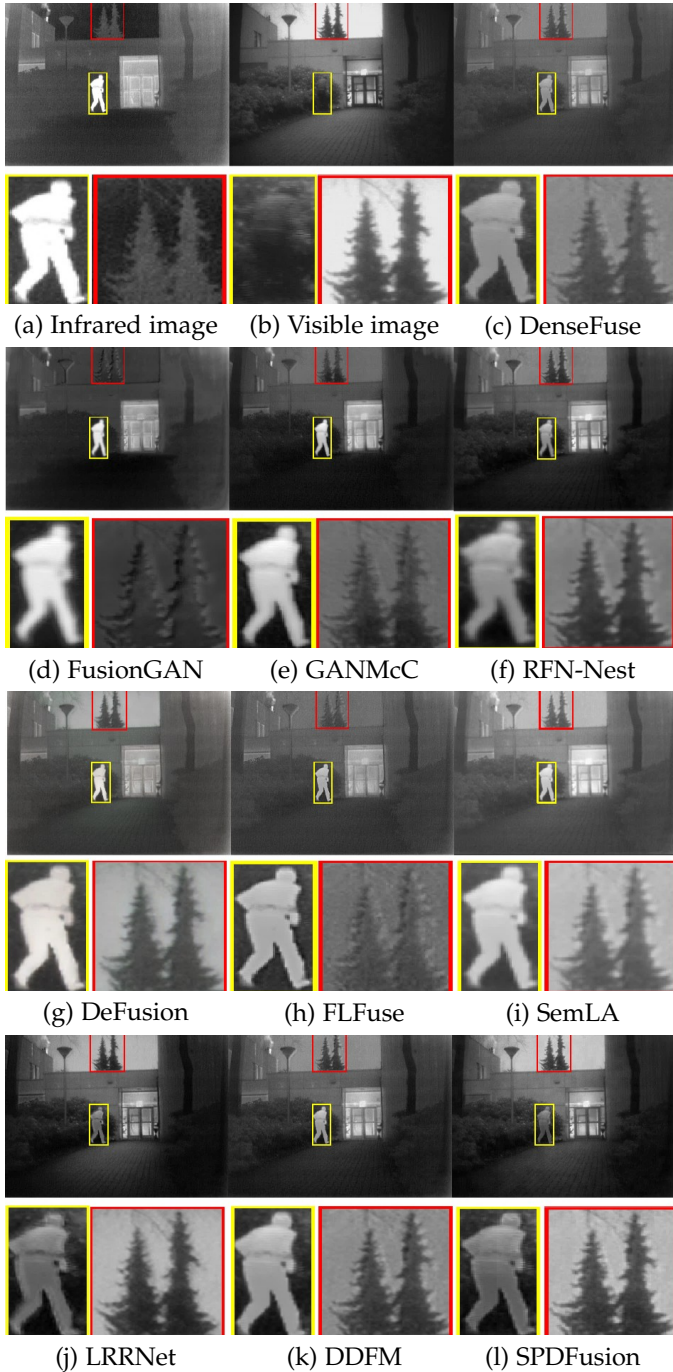


Fig. 6: Infrared and visible image fusion experiment on TNO dataset.

layers. Within the manifold module, the SGD optimizer on the Stiefel manifold was used to update the weights of the BiMap layer, with a learning rate set to 0.01. For the convolutional layers, we used the Adam optimizer to update the weights, with the learning rate for this part set to 0.0001.

At the same time, in our loss function, the parameters  $\alpha, \beta, \gamma$  are set to 1, 10, 20, respectively, to achieve the best fusion effect.

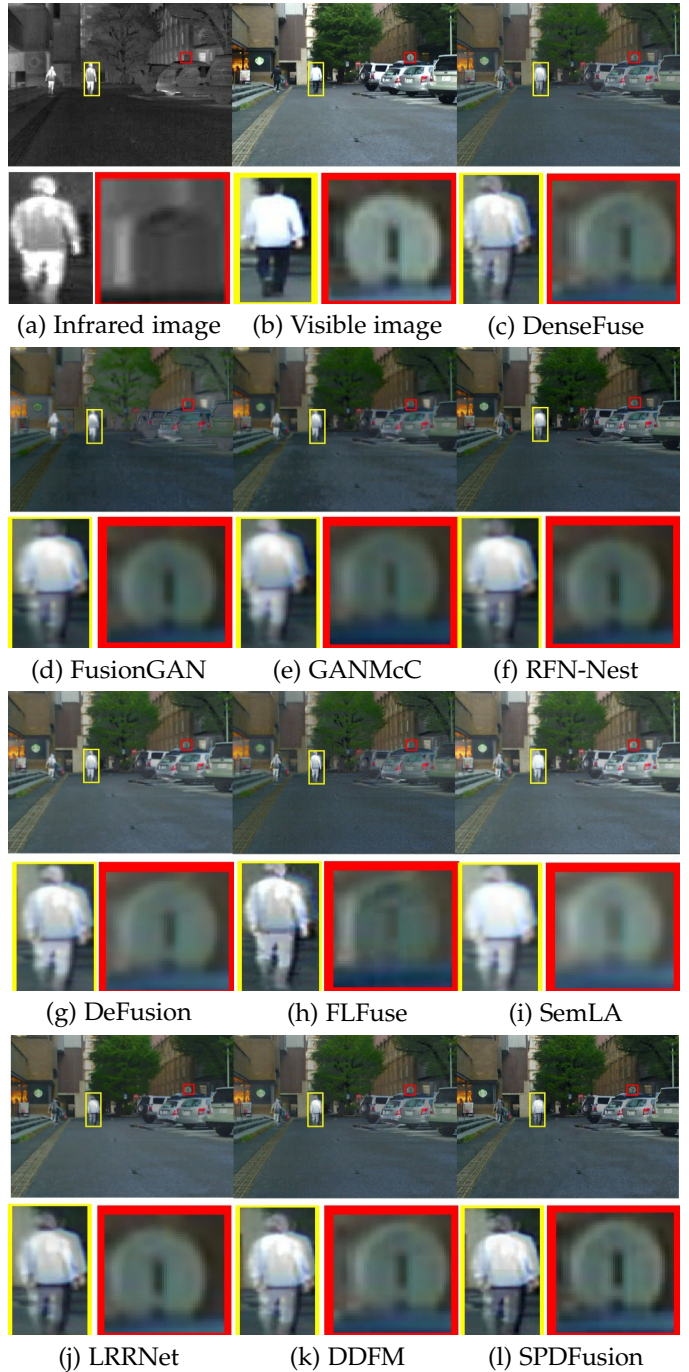


Fig. 7: Infrared and visible image fusion experiment on MSRS dataset.

#### 4.1.3 The Methods Compared and the Quality Metrics Used.

The method presented in this article was compared and evaluated with nine different state-of-the-art image fusion network approaches, including some classic and latest methods. These are: GANMcC [34], DenseFuse [35], FusionGAN [36], SemLA [37], FLFuse [38], RFN-Nest [13], DeFusion [39], DDFM [40] and LRRNet [8]. Regarding the quality metrics, seven indices were chosen for performance evaluation, including: Entropy (En), Mutual Information (MI), Standard Deviation (SD), Spatial Frequency (SF), Vi-



sual Information Fidelity (VIF), Average Gradient (AG),  $Q^{AB/F}$ . These indices measure the overall quality of images from different perspectives.

## 4.2 Comparative Results Analysis

In this section, we conduct both qualitative and quantitative experiments with the proposed SPDFusion using two classical infrared-visible light datasets, TNO and MSRS, to verify the performance of our method.

### 4.2.1 The Fusion Results on TNO

First, we conduct experiments on the TNO dataset, by comparing all the methods on an image called "man", which is shown in Fig. 6.

It is worth mentioning that for the parts of the image involving the tree tops and the sky, as indicated by the red highlighted areas, previous methods such as DenseFuse, FusionGAN, GANMcC, and FLFuse were unable to maintain the original color features and texture details of the images. In comparison, although RFN-Nest and SemLA provided some improvements in brightness and details in the visible light, their capacity to preserve essential details in edge areas, like pedestrian outlines, remained a problem. Meanwhile, the latest three methods, DeFusion, LRRNet, and DDFM, perform well in these aspects, but it is still difficult to achieve a balance between capturing high correlation scene information and obtaining low correlation semantic information in different modalities. Our SPDFusion enhanced the clarity and brightness of the image in areas where the background is more indistinct. On the other hand, in the parts concerning the targeted individuals, as shown by the yellow highlighted areas, our approach was able to offer clearer delineation of the edge regions, resulting in higher contrast, while also conforming to human visual perception.

Additionally, we utilized the previous seven indices to conduct an objective evaluation of the methods mentioned above. As shown in the Table 1, the first and the second optimal results are marked with bold and red font respectively. Among the various state-of-the-art fusion methods, SPDFusion achieved the highest level in five classic image fusion metrics (EN, SD, SF, VIF, AG) and reached the second-highest level in the remaining two metrics (MI,  $Q^{AB/F}$ ). These results indicate that our method not only enhances the overall sharpness of the image but also presents a more balanced and realistic visual effect, significantly surpassing existing technologies in terms of visual quality.

### 4.2.2 Fusion Results on MSRS

To verify the generalization performance of our SPDFusion, we selected more IR-VI pairs from the MSRS dataset for analysis and comparison, as shown in Fig. 7. Compared to methods like FusionGAN, GANMcC, RFN-Nest, SemLA and DeFusion, our SPDFusion method highlights infrared targets and performs visual enhancement more distinctively, as illustrated by the yellow boxed sections in the images. This to some extent reflects that the Riemannian attention mechanism can capture deep statistical information across different modalities effectively. At the same time, fusion images generated by DenseFuse, FLFuse, LRRNet and DDFM



Fig. 8: The qualitative results obtained using unimodal and multimodal fusion strategies.

appear relatively blurry, whereas our method retains more detailed parts of the objects within the scene (as indicated by the red boxed sections in the images). This means that our method preserves not only the prominent features from the infrared image but also the texture details from the visible light image, which is crucial for the task of image fusion.

In the Table 2, compared to other fusion methods, our proposed SPDFusion achieved the best values in four metrics (SD, SF, AG,  $Q^{AB/F}$ ) and the second-best in one metric (VIF). This indicates that the images fused via SPDFusion contain more edge details and have a higher degree of information fidelity, also reflecting our work's success in achieving cross-modal pixel and semantic-level fusion.

## 4.3 Ablation Study

In this section, we objectively analyze the effectiveness of several modules in our work and conduct a comparative analysis addressing the following aspects: the fusion strategies, different layer structures of SPD-block, the rationality of manifold attention and selection of different  $\epsilon$  values.

### 4.3.1 Different fusion strategies

In this section, we discussed in detail how different fusion strategies affect the fusion results and compared them from subjective and objective perspectives. "cross-modal strategy" refers to a fusion strategy that computes the covariance matrices of two modalities, while "single-modal strategy" refers to computing the covariance matrices of each modality individually. Table 3 presents the average values of five metrics, with the best values shown in bold. From a quantitative perspective, the cross-modal fusion strategy exhibits better performance in all five metrics: EN, SD, SF, VIF, and AG. This demonstrates that the design of our fusion strategy is beneficial in making the fused images visually closer to real scenes, effectively preserving the rich texture details of the source images. Therefore, in our framework, we adopt a cross-modal fusion strategy to integrate information from multiple source images and generate high-definition fused images. Some examples of the fusion results obtained using different fusion strategies are shown in Fig. 8.

### 4.3.2 Different Layer Structures of SPD-Block

When processing data on Riemannian manifolds, each layer of BiMap and ReEig signifies a transformation of the Riemannian manifold. The processing of each layer needs to

TABLE 1: Quantitative Experiments on the TNO Dataset.

Methods	Year	EN	MI	SD	SF	VIF	AG	Qabf
DenseFuse	2019	6.380	2.227	25.259	6.570	0.574	2.569	0.349
FusionGAN	2019	6.551	2.330	30.416	6.306	0.413	2.422	0.230
GANMcC	2021	6.735	2.276	33.361	6.189	0.520	2.553	0.277
RFN-Nest	2021	6.971	2.126	37.090	5.931	0.550	2.691	0.333
DeFusion	2022	6.607	<b>2.627</b>	30.868	6.461	0.559	2.624	0.365
FLFuse	2023	6.388	2.177	25.600	6.767	0.603	2.622	0.395
SemLA	2023	6.879	2.051	37.890	8.528	0.470	2.892	0.265
LRRNet	2023	<b>6.991</b>	2.518	<b>40.984</b>	<b>9.608</b>	0.548	<b>3.790</b>	0.352
DDFM	2023	6.854	2.231	34.418	8.629	<b>0.631</b>	3.405	<b>0.434</b>
SPDFusion	Ours	<b>7.055</b>	<b>2.540</b>	<b>41.936</b>	<b>9.655</b>	<b>0.645</b>	<b>3.973</b>	<b>0.405</b>

TABLE 2: Quantitative Experiments on the MSRS Dataset.

Methods	Years	EN	MI	SD	SF	VIF	AG	Qabf
DenseFuse	2019	5.931	2.666	23.550	6.020	0.692	2.053	0.368
FusionGAN	2019	5.431	1.893	17.076	4.354	0.442	1.452	0.140
GANMcC	2021	6.120	2.565	26.356	5.664	0.635	2.006	0.302
RFN-Nest	2021	6.196	2.460	29.078	6.163	0.656	2.115	0.390
DeFusion	2022	<b>6.383</b>	<b>2.990</b>	<b>35.429</b>	8.146	0.730	<b>2.654</b>	<b>0.507</b>
FLFuse	2023	5.754	2.134	19.469	4.841	0.651	1.815	0.289
SemLA	2023	<b>6.423</b>	2.461	33.122	6.351	0.617	2.257	0.290
LRRNet	2023	6.192	<b>2.928</b>	31.758	<b>8.473</b>	0.541	2.651	0.454
DDFM	2023	6.175	2.735	28.925	7.388	<b>0.743</b>	2.522	0.474
SPDFusion	Ours	6.362	2.786	<b>35.746</b>	<b>8.928</b>	<b>0.740</b>	<b>2.878</b>	<b>0.524</b>

maintain the topological characteristics of the data, that is, to preserve the proximity and the interrelations between data points. If the structural properties of the original Riemannian manifold are lost during the multi-layer processing, the quality of the final fusion will decrease.

Deep architectures may not always exhibit optimal performance in low-level visual tasks such as image fusion. Therefore, we attempted to train using different manifold network structures. As shown in Table 3 and Fig. 9, when the number of layers of BiMap and ReEig is only set to 1, the features of the original data are faithfully preserved through single-layer transformation, reducing the distortion or information loss that may occur in the features after multi-layer mapping. Meanwhile, as the number of layers in the SPD network increases, the gradient update may bias towards the deep semantic features within the modality due to their larger variance, while fusion tasks often require more attention to pixel-level information. Therefore, in our work, we adopt a layer of BiMap and ReEig to achieve the best performance.

### 4.3.3 Manifold Attention

In this section, we assess the effectiveness of SPDAM by using different network architectures, as illustrated in Table 3. We replaced our attention module with four of the most popular network structures currently available, including the relatively classic network architecture (DenseNet) and attention-based network architectures (SENet, CBAM, Transformer). For a more intuitive comparison, we visualize both the source images and the fused images from different methods. As shown in Fig. 10, compared to previous traditional methods, our SPDFusion enhances the texture features of shrubbery and trees and also highlights the detail features of the pedestrian area in the infrared modality. In

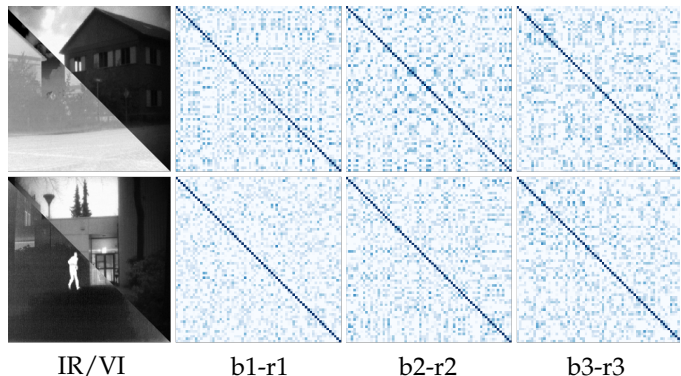


Fig. 9: Visualization results of intermediate covariance matrices obtained from different manifold layer structures. The size of each covariance matrix is 1089×1089.

addition, in our example, highly relevant parts like the sky have been significantly enhanced.

At the same time, we also conducted a quantitative comparative experiment to further demonstrate the effectiveness of our SPDAM in the fusion task. As shown in Table 3, our module surpasses other methods in terms of EN, SD, and VIF indicators, indicating that under the iteration of the Riemannian network, the network has deepened its focus on the associated information of the salient parts within modalities. Moreover, it emphasizes the useful complementary information between different modalities, promoting fusion with high contrast and detailed preservation.

### 4.3.4 Setting the Size of $\epsilon$

Equation 3 enhances the discriminative of SPD matrices through the correction of small eigenvalues. Since the shortest path between points on a Riemannian manifold is repre-

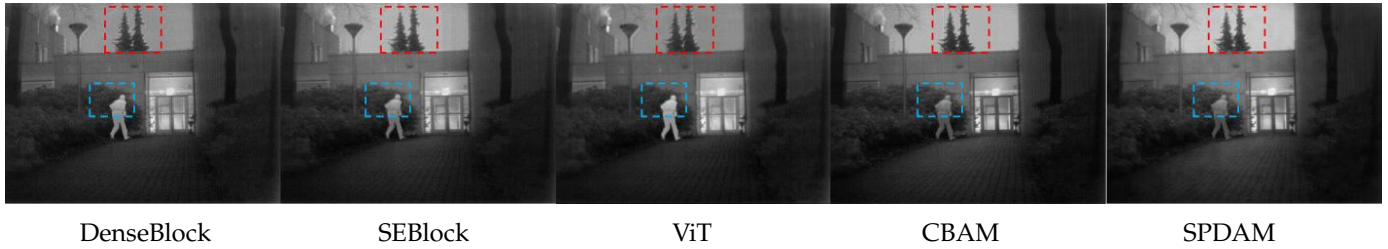


Fig. 10: Infrared and visible image fusion experiment on the TNO dataset.

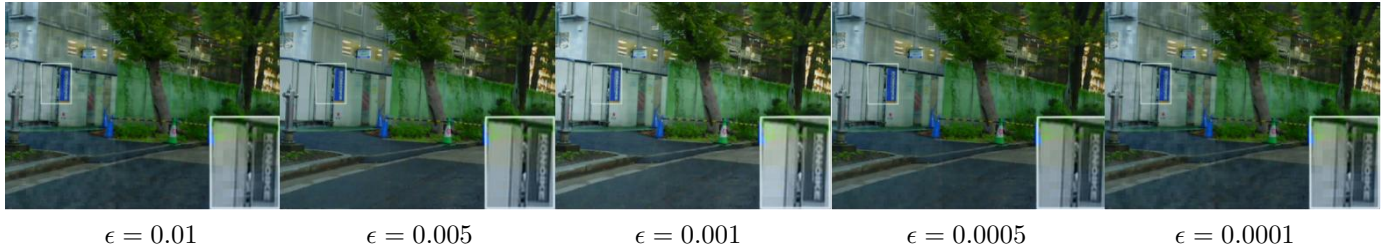


Fig. 11: Visualization of the impact of different  $\epsilon$  values on the fusion results.

TABLE 3: Objective results of ablation study. Here, "b2-r2" and "b3-r3" represent the number of blocks in BiMap and ReEig, respectively. "single-modal strategy(ir)" and "single-modal strategy(vi)" indicate the modal information contained within the SPD matrix that needs to be learned. " $F_{Dense}$ ", " $F_{SE}$ ", " $F_{CBAM}$ ", " $F_{ViT}$ " denote that our SPDAM is replaced by Dense Block, SE Block, CBAM, and ViT structures, respectively. " $\epsilon$ " is a perturbation applied to the images.

	EN	SD	SF	VIF	AG
Ours(b1-r1)	<b>7.055</b>	<b>41.936</b>	9.655	<b>0.645</b>	3.973
b2-r2	6.995	38.224	8.762	0.552	3.761
b3-r3	6.979	37.575	8.758	0.550	3.788
single-modal strategy(ir)	6.951	36.343	8.583	0.529	3.727
single-modal strategy(vi)	7.024	38.733	8.564	0.527	3.675
$F_{Dense}$	6.914	35.626	9.072	0.592	<b>3.987</b>
$F_{SE}$	7.003	38.893	7.954	0.520	3.520
$F_{CBAM}$	6.927	36.296	6.524	0.506	2.827
$F_{ViT}$	6.906	37.356	<b>9.662</b>	0.633	3.799
$\epsilon=0.01$	6.969	37.749	9.080	0.589	3.871
$\epsilon=0.0001$	7.010	36.917	8.319	0.406	3.637
$\epsilon=0.0005$	6.975	37.896	9.075	0.583	3.883
$\epsilon=0.0005$	6.976	37.028	8.707	0.511	3.784

sented by geodesic distance, the epsilon setting in the ReEig layer is effectively adjusting the curvature on the manifold, thereby affecting the representation of local contrast and textural information in images. If  $\epsilon$  is too large, it may cause data points to shift excessively on the manifold, resulting in the loss of the original geometric structure. Conversely, if  $\epsilon$  is too small, it may lead to certain edge or detail features not being emphasized, making it difficult for the fused image to capture important information from different modalities. Therefore, we conduct an ablation study to determine the effect of different values of  $\epsilon$ . Their values are set as follows:  $\epsilon \in \{1e^{-2}, 5e^{-3}, 1e^{-3}, 5e^{-4}, 1e^{-4}\}$ .

As shown in Fig. 11, we selected an instance from the MSRS dataset for intuitive demonstration. When  $\epsilon$  is set to  $1e^{-2}$  and  $1e^{-4}$ , the image exhibits obvious block artifacts due to uneven SPD weight distribution, which affects the visual quality of the image. When  $\epsilon$  is set to  $5e^{-3}$  and  $5e^{-4}$ , the left part of the image has many details submerged in darkness, failing to provide effective scene brightness

information. When  $\epsilon$  is set to  $1e^{-3}$ , the fused image achieves the optimal effect.

Therefore, in the subsequent experiments, we set our  $\epsilon$  to  $1e^{-2}$ .

#### 4.4 Experiments in Object Detection

##### 4.4.1 Quantitative Comparisons

We performed an evaluation of the previously mentioned fusion networks using YOLOv7 [41]. The results were measured by the object detection metrics, namely: accuracy, recall, mean precision at 0.5 (AP50), and mean precision at 0.5:0.95 (AP50:95). As shown in Table 4, our method achieved the highest performance on three metrics, and secured the second-best performance on two detection metrics.

##### 4.4.2 Qualitative Comparisons

In terms of visual effects, our method also has significant advantages, as shown in Fig. 12. In the examples of tradition

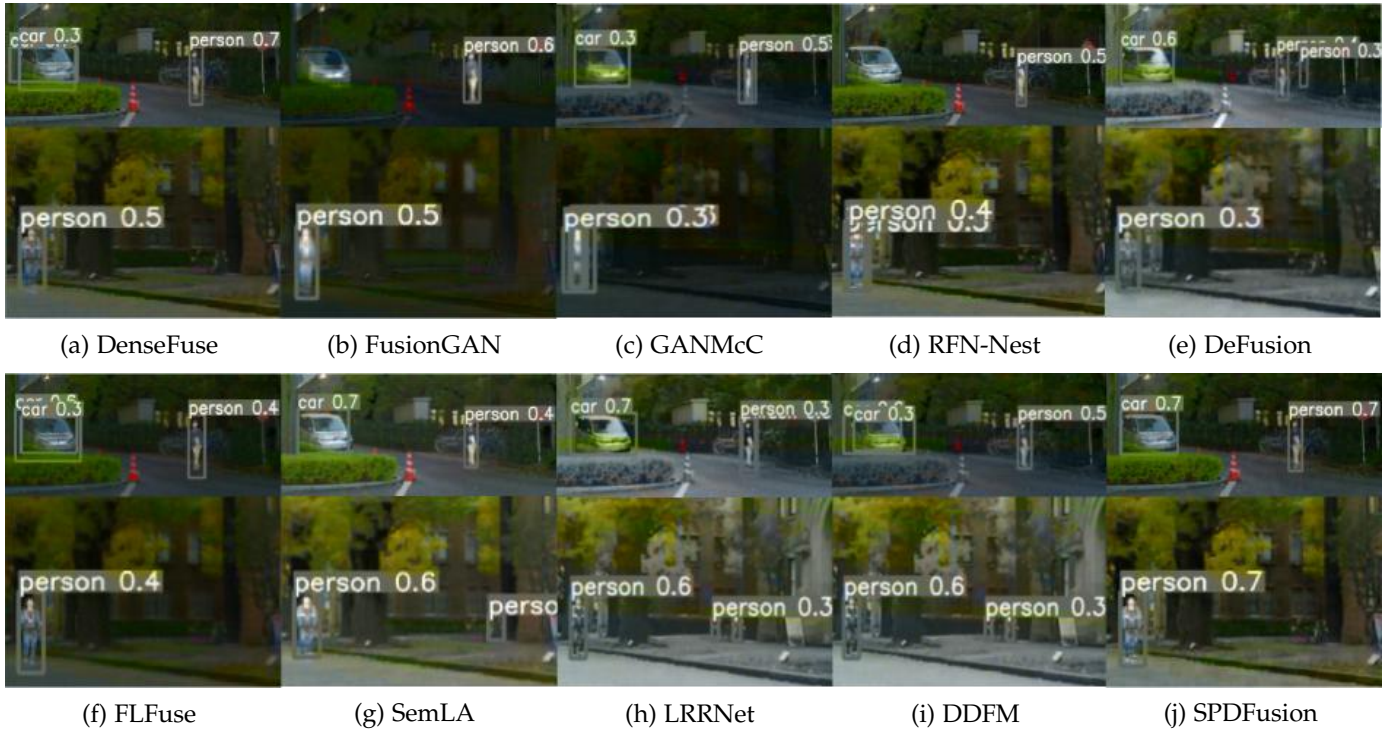


Fig. 12: Object detection results compared with other state-of-the-art fusion methods.

TABLE 4: Quantitative evaluation of object detection using the MSRS dataset.

Methods	Year	Person	Car	All	Recall	mAP@0.5	mAP@0.5:0.95
DenseFuse	2019	<b>1.000</b>	0.874	<b>0.937</b>	0.319	0.518	0.287
FusionGAN	2019	0.889	0.615	0.752	0.481	0.578	0.362
GANMcC	2021	0.609	<b>0.883</b>	0.746	<b>0.705</b>	0.784	0.424
RFN-Nest	2021	0.760	0.633	0.696	0.569	0.592	0.307
DeFusion	2022	0.882	0.696	0.789	0.690	<b>0.825</b>	0.473
FLFuse	2023	0.894	<b>0.893</b>	0.894	0.671	0.777	0.462
SemLA	2023	0.857	0.771	0.814	0.653	0.732	0.430
LRRNet	2023	0.850	0.634	0.742	0.671	0.797	0.469
DDFM	2023	<b>0.932</b>	0.801	0.867	0.629	<b>0.810</b>	<b>0.483</b>
SPDFusion	Ours	<b>1.000</b>	0.879	<b>0.939</b>	<b>0.695</b>	<b>0.810</b>	<b>0.491</b>

methods, FusionGAN and RFN-Nest failed to detect the car, while DenseFuse, LRRNet and DDFM exhibited cases of redundant detection without accurately distinguishing the targets. When the picture shows night scenes with dim lighting, both GANMcC and FLFuse exhibit lower accuracy rates. Although DeFusion and SemLA have done well in the above aspects, false positives in regions with unclear edges have led to less than ideal detection results. In contrast, our SPDFusion maintained high detection accuracy in these challenging scenarios, preserving the prominent features and texture details of the targets, which further verifies the superiority of our approach.

### 5 CONCLUSION

Previous image fusion methods have primarily focused on computational processes that rely on Euclidean metric feature representations. Consequently, the intrinsic Riemannian of images have been ignored, resulting in the loss of some discriminative information when combining data from different modalities.

In this paper, a pioneering approach is taken by modeling images onto the Riemannian SPD manifold and designing a non-Euclidean statistical correlation coding strategy. In this scenario, the source images are divided into small tokens and projected into the SPD network for manifold learning. This approach not only captures salient semantic information contained within each modality more effectively, but also enhances the model’s overall perception of deep statistical information association between modalities.

Our attention module is designed based on the principle of convolution, using the covariance matrix as a weight matrix, which is then multiplied by the row vector matrix of the image. During this process, by utilizing the learned covariance matrix to adjust the weights of each pixel or pixel region, we can modulate the degree of “attention” allocation to the image. This allocation mechanism reflects the intrinsic Riemannian geometrical structure of the image.

The results obtained on public datasets indicate that our approach preserves more detail features of visible light images and enhances the salient information of the infrared component, compared to existing fusion networks.

Our fusion method has been applied to other computer vision tasks, such as object detection, and exhibited superior performance compared to other popular approaches as well.

In this work, we have only discussed one effective design of the SPD manifold in fusion tasks. It cannot be overemphasised that the research space for cross-modal fusion tasks based on manifold learning remains vastly expansive. In the future, we will continue to explore new methods for solving classical computer vision tasks using other manifolds.

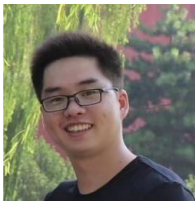
## REFERENCES

- [1] H. Xu and J. Ma, "Emfusion: An unsupervised enhanced medical image fusion network," *Information Fusion*, vol. 76, pp. 177–186, 2021.
- [2] Y. Li, J. Zhao, Z. Lv, and J. Li, "Medical image fusion method by deep learning," *International Journal of Cognitive Computing in Engineering*, vol. 2, pp. 21–29, 2021.
- [3] J. Ma, W. Yu, C. Chen, P. Liang, X. Guo, and J. Jiang, "Pan-gan: An unsupervised pan-sharpening method for remote sensing image fusion," *Information Fusion*, vol. 62, pp. 110–120, 2020.
- [4] C. Zhang, P. Yue, D. Tapete, L. Jiang, B. Shanguan, L. Huang, and G. Liu, "A deeply supervised image fusion network for change detection in high resolution bi-temporal remote sensing images," *ISPRS Journal of Photogrammetry and Remote Sensing*, vol. 166, pp. 183–200, 2020.
- [5] L. Tang, J. Yuan, and J. Ma, "Image fusion in the loop of high-level vision tasks: A semantic-aware real-time infrared and visible image fusion network," *Information Fusion*, vol. 82, pp. 28–42, 2022.
- [6] J. Chen, X. Li, L. Luo, X. Mei, and J. Ma, "Infrared and visible image fusion based on target-enhanced multiscale transform decomposition," *Information Sciences*, vol. 508, pp. 64–78, 2020.
- [7] H. Li, X.-J. Wu, and J. Kittler, "Mdlatrr: A novel decomposition method for infrared and visible image fusion," *IEEE Transactions on Image Processing*, vol. 29, pp. 4733–4746, 2020.
- [8] H. Li, T. Xu, X.-J. Wu, J. Lu, and J. Kittler, "Lrrnet: A novel representation learning guided fusion network for infrared and visible images," *IEEE transactions on pattern analysis and machine intelligence*, 2023.
- [9] H. Zhang, H. Xu, X. Tian, J. Jiang, and J. Ma, "Image fusion meets deep learning: A survey and perspective," *Information Fusion*, vol. 76, pp. 323–336, 2021.
- [10] K. Chen, S. Liu, T. Zhu, J. Qiao, Y. Su, Y. Tian, et al., "Improving expressivity of gnns with subgraph-specific factor embedded normalization," in *Proceedings of the 29th ACM SIGKDD Conference on Knowledge Discovery and Data Mining*, 2023.
- [11] K. Chen, J. Song, S. Liu, N. Yu, Z. Feng, G. Han, and M. Song, "Distribution knowledge embedding for graph pooling," 2022.
- [12] Y. Zhang, Y. Liu, P. Sun, H. Yan, X. Zhao, and L. Zhang, "Ifcnn: A general image fusion framework based on convolutional neural network," *Information Fusion*, vol. 54, pp. 99–118, 2020.
- [13] H. Li, X.-J. Wu, and J. Kittler, "Rfn-nest: An end-to-end residual fusion network for infrared and visible images," *Information Fusion*, vol. 73, pp. 72–86, 2021.
- [14] Y. Liu, L. Wang, J. Cheng, C. Li, and X. Chen, "Multi-focus image fusion: A survey of the state of the art," *Information Fusion*, vol. 64, pp. 71–91, 2020.
- [15] Y. Liu, X. Chen, H. Peng, and Z. Wang, "Multi-focus image fusion with a deep convolutional neural network," *Information Fusion*, vol. 36, pp. 191–207, 2017.
- [16] A. Dosovitskiy, L. Beyer, A. Kolesnikov, D. Weissenborn, X. Zhai, T. Unterthiner, M. Dehghani, M. Minderer, G. Heigold, S. Gelly, et al., "An image is worth 16x16 words," *arXiv preprint arXiv:2010.11929*, vol. 7, 2020.
- [17] L. Qu, S. Liu, M. Wang, and Z. Song, "Transmef: A transformer-based multi-exposure image fusion framework using self-supervised multi-task learning," in *Proceedings of the AAAI conference on artificial intelligence*, vol. 36, pp. 2126–2134, 2022.
- [18] J. Ma, L. Tang, F. Fan, J. Huang, X. Mei, and Y. Ma, "Swinfusion: Cross-domain long-range learning for general image fusion via swin transformer," *IEEE/CAA Journal of Automatica Sinica*, vol. 9, no. 7, pp. 1200–1217, 2022.
- [19] Z. Zhao, H. Bai, J. Zhang, Y. Zhang, S. Xu, Z. Lin, R. Timofte, and L. Van Gool, "Cddfuse: Correlation-driven dual-branch feature decomposition for multi-modality image fusion," in *Proceedings of the IEEE/CVF conference on computer vision and pattern recognition*, pp. 5906–5916, 2023.
- [20] H. Xu, J. Yuan, and J. Ma, "Murf: Mutually reinforcing multi-modal image registration and fusion," *IEEE transactions on pattern analysis and machine intelligence*, 2023.
- [21] R. Wang, H. Guo, L. S. Davis, and Q. Dai, "Covariance discriminative learning: A natural and efficient approach to image set classification," in *2012 IEEE conference on computer vision and pattern recognition*, pp. 2496–2503, IEEE, 2012.
- [22] R. Wang, X.-J. Wu, Z. Chen, T. Xu, and J. Kittler, "Learning a discriminative spd manifold neural network for image set classification," *Neural networks*, vol. 151, pp. 94–110, 2022.
- [23] R. Wang, X.-J. Wu, and J. Kittler, "Symnet: A simple symmetric positive definite manifold deep learning method for image set classification," *IEEE Transactions on Neural Networks and Learning Systems*, vol. 33, no. 5, pp. 2208–2222, 2022.
- [24] Z. Chen, Y. Song, G. Liu, R. R. Kompella, X. Wu, and N. Sebe, "Riemannian multiclass logistics regression for spd neural networks," *arXiv preprint arXiv:2305.11288*, 2023.
- [25] Z. Huang and L. Van Gool, "A riemannian network for spd matrix learning," in *Proceedings of the AAAI conference on artificial intelligence*, vol. 31, 2017.
- [26] D. Brooks, O. Schwander, F. Barbaresco, J.-Y. Schneider, and M. Cord, "Riemannian batch normalization for spd neural networks," *Advances in Neural Information Processing Systems*, vol. 32, 2019.
- [27] X. Wang, R. Girshick, A. Gupta, and K. He, "Non-local neural networks," in *Proceedings of the IEEE conference on computer vision and pattern recognition*, pp. 7794–7803, 2018.
- [28] H. Zhang, I. Goodfellow, D. Metaxas, and A. Odena, "Self-attention generative adversarial networks," in *International conference on machine learning*, pp. 7354–7363, PMLR, 2019.
- [29] J. Hu, L. Shen, and G. Sun, "Squeeze-and-excitation networks," in *Proceedings of the IEEE conference on computer vision and pattern recognition*, pp. 7132–7141, 2018.
- [30] S. Woo, J. Park, J.-Y. Lee, and I. S. Kweon, "Cbam: Convolutional block attention module," in *Proceedings of the European conference on computer vision (ECCV)*, pp. 3–19, 2018.
- [31] K. Simonyan and A. Zisserman, "Very deep convolutional networks for large-scale image recognition," *arXiv preprint arXiv:1409.1556*, 2014.
- [32] L. Tang, J. Yuan, H. Zhang, X. Jiang, and J. Ma, "Piafusion: A progressive infrared and visible image fusion network based on illumination aware," *Information Fusion*, vol. 83, pp. 79–92, 2022.
- [33] A. Toet and M. A. Hogervorst, "Progress in color night vision," *Optical Engineering*, vol. 51, no. 1, pp. 010901–010901, 2012.
- [34] J. Ma, H. Zhang, Z. Shao, P. Liang, and H. Xu, "Ganmcc: A generative adversarial network with multiclassification constraints for infrared and visible image fusion," *IEEE Transactions on Instrumentation and Measurement*, vol. 70, pp. 1–14, 2020.
- [35] H. Li and X.-J. Wu, "Densefuse: A fusion approach to infrared and visible images," *IEEE Transactions on Image Processing*, vol. 28, no. 5, pp. 2614–2623, 2018.
- [36] J. Ma, W. Yu, P. Liang, C. Li, and J. Jiang, "Fusiongan: A generative adversarial network for infrared and visible image fusion," *Information fusion*, vol. 48, pp. 11–26, 2019.
- [37] H. Xie, Y. Zhang, J. Qiu, X. Zhai, X. Liu, Y. Yang, S. Zhao, Y. Luo, and J. Zhong, "Semantics lead all: Towards unified image registration and fusion from a semantic perspective," *Information Fusion*, vol. 98, p. 101835, 2023.
- [38] W. Xue, A. Wang, and L. Zhao, "Ifuse-net: A fast and lightweight infrared and visible image fusion network via feature flow and edge compensation for salient information," *Infrared Physics & Technology*, vol. 127, p. 104383, 2022.
- [39] P. Liang, J. Jiang, X. Liu, and J. Ma, "Fusion from decomposition: A self-supervised decomposition approach for image fusion," in *European Conference on Computer Vision*, pp. 719–735, Springer, 2022.
- [40] Z. Zhao, H. Bai, Y. Zhu, J. Zhang, S. Xu, Y. Zhang, K. Zhang, D. Meng, R. Timofte, and L. Van Gool, "Ddfm: denoising diffusion model for multi-modality image fusion," in *Proceedings of the IEEE/CVF International Conference on Computer Vision*, pp. 8082–8093, 2023.

- [41] C.-Y. Wang, A. Bochkovskiy, and H.-Y. M. Liao, "Yolov7: Trainable bag-of-freebies sets new state-of-the-art for real-time object detectors," in *Proceedings of the IEEE/CVF conference on computer vision and pattern recognition*, pp. 7464–7475, 2023.



**Huan Kang** received the B.E. degree in software engineering from Jiangsu University of Science and Technology, China. He is currently a Master student in the Jiangsu Provincial Engineering Laboratory of Pattern Recognition and Computational Intelligence Jiangnan University. His research interests include image fusion, machine learning and deep learning.



**Hui Li** received the B.Sc. degree in School of Internet of Things Engineering from Jiangnan University, China, in 2015. He received the PhD degree at the School of Internet of Things Engineering, Jiangnan University, Wuxi, China, in 2022. He is currently a Lecturer at the School of Artificial Intelligence and Computer Science, Jiangnan University, Wuxi, China. His research interests include image fusion and multi-modal visual information processing. He has been chosen among the World's Top 2% Scientists ranking in the single recent year dataset published by Stanford University (2022 and 2023).

He has published several scientific papers, including IEEE TPAMI, IEEE TIP, Information Fusion, IEEE TCYB, IEEE TIM, ICPR etc. He achieved top tracking performance in several competitions, including the VOT2020 RGBT challenge (ECCV20) and Anti-UAV challenge (ICCV21).



**Tianyang Xu** received the B.Sc. degree in electronic science and engineering from Nanjing University, Nanjing, China, in 2011. He received the PhD degree at the School of Artificial Intelligence and Computer Science, Jiangnan University, Wuxi, China, in 2019. He is currently an Associate Professor at the School of Artificial Intelligence and Computer Science, Jiangnan University, Wuxi, China. His research interests include visual tracking and deep learning. He has published several scientific papers, including

IEEE TPAMI, IJCV, ICCV, TIP, TIFS, TKDE, AAAI etc. He achieved top 1 performance in several competitions, including VOT2020 RGBT challenge (ECCV20), Anti-UAV challenge (CVPR20), MMVRAC challenges (ICCV2021).



**Rui Wang** received the M.S. degree in computer science from Jiangnan University, Wuxi, China, in 2018, and the Ph.D. degree in pattern recognition and intelligent system from Jiangnan University, Wuxi, China, in 2023. He is currently a Lecturer with the School of Artificial Intelligence and Computer Science, Jiangnan University. He has published several scientific papers, including IEEE TRANSACTIONS ON NEURAL NETWORKS AND LEARNING SYSTEMS, IEEE TRANSACTIONS ON MULTIMEDIA, IEEE TRANSACTIONS ON CIRCUITS AND SYSTEMS FOR VIDEO TECHNOLOGY, IEEE TRANSACTIONS ON BIG DATA, IEEE TRANSACTIONS ON COGNITIVE AND DEVELOPMENTAL SYSTEMS, Neural Networks, Neural Processing Letters, AAAI Conference on Artificial Intelligence, International Conference on Pattern Recognition, and Asian Conference on Computer Vision. His research interests include Riemannian manifold learning, metric learning, and deep learning.



**Xiao-Jun Wu** received his B.S. degree in mathematics from Nanjing Normal University, Nanjing, PR China in 1991 and M.S. degree in 1996, and Ph.D. degree in Pattern Recognition and Intelligent System in 2002, both from Nanjing University of Science and Technology, Nanjing, PR China, respectively. He was a fellow of United Nations University, International Institute for Software Technology (UNU/IIST) from 1999 to 2000. From 1996 to 2006, he taught in the School of Electronics and Information, Jiangsu

University of Science and Technology where he was an exceptionally promoted professor. He joined Jiangnan University in 2006 where he is currently a distinguished professor in the School of Artificial Intelligence and Computer Science, Jiangnan University. He won the most outstanding postgraduate award by Nanjing University of Science and Technology. He has published more than 400 papers in his fields of research. He was a visiting postdoctoral researcher in the Centre for Vision, Speech, and Signal Processing (CVSSP), University of Surrey, UK from 2003 to 2004, under the supervision of Professor Josef Kittler. His current research interests are pattern recognition, computer vision, fuzzy systems, and neural networks. He owned several domestic and international awards because of his research achievements. Currently, he is a Fellow of IAPR and AAAI. His current research interests include pattern recognition, computer vision, fuzzy systems, neural networks and intelligent systems.



**Josef Kittler** (Life Member, IEEE) received the B.A., Ph.D., and D.Sc. degrees from the University of Cambridge, Cambridge, U.K., in 1971, 1974, and 1991, respectively. He is currently a Distinguished Professor of machine intelligence with the Centre for Vision, Speech and Signal Processing, University of Surrey, Guildford, U.K. He conducts research in biometrics, video and image database retrieval, medical image analysis, and cognitive vision. He has authored or coauthored the textbook *Pattern Recognition: A*

*Statistical Approach* and over 700 scientific papers. Dr. Kittler served as a member of the Editorial Board for the IEEE TRANSACTIONS ON PATTERN ANALYSIS AND MACHINE INTELLIGENCE from 1982 to 1985. He also served on the Governing Board for the International Association for Pattern Recognition (IAPR) as one of the two British representatives from 1982 to 2005 and the President of the IAPR from 1994 to 1996. He is a Series Editor of *Lecture Notes in Computer Science* (Springer). He currently serves on the Editorial Board of *Pattern Recognition Letters*, *Pattern Recognition and Artificial Intelligence*, and *Pattern Analysis and Applications*. His publications have been cited more than 65 000 times (Google Scholar).